Image Correlation Spectroscopy with Second Harmonic Generating Nanoparticles in Suspension and in Cells

Peer-reviewed author version

SLENDERS, Eli; Boye, Hannelore; Urbain, Mathias; Mugnier, Yannick; Sonay, Ali Yasin; Pantazis, Periklis; Bonacina, Luigi; Berghe, Pieter Vanden; vandeVen, Martin & AMELOOT, Marcel (2018) Image Correlation Spectroscopy with Second Harmonic Generating Nanoparticles in Suspension and in Cells. In: JOURNAL OF PHYSICAL CHEMISTRY LETTERS, 9(20), p. 6112-6118.

DOI: 10.1021/acs.jpclett.8b02686
Handle: http://hdl.handle.net/1942/28059

Image Correlation Spectroscopy with Second Harmonic Generating nanoparticles in suspension and in cells

Eli Slenders,[†] Hannelore Bové,[†] Mathias Urbain,[‡] Yannick Mugnier,[‡] Ali Yasin Sonay,[¶] Periklis Pantazis,[¶] Luigi Bonacina,[§] Pieter Vanden Berghe,[‖] Martin vandeVen,[†] and Marcel Ameloot[*,†]

†*Biomedical Research Institute (BIOMED), Hasselt University, Agoralaan Bldg. C, 3590 Diepenbeek, Belgium*

‡*Univ. Savoie Mont Blanc, SYMME, F–74000, Annecy, France*

¶*Department of Biosystems Science and Engineering, ETH Zürich, Mattenstrasse 26, 4058 Basel, Switzerland*

§*Department of Applied Physics, Université de Genève, Chemin de Pinchat 22, Geneva, Switzerland*

‖*Laboratory for Enteric Neuroscience (LENS), TARGID, University of Leuven, Herestraat 49, 3000 Leuven, Belgium*

E-mail: marcel.ameloot@uhasselt.be

Phone: +32 (0)11 26 92 33. Fax: +32 (0)11 26 92 99

Abstract

The absence of photobleaching, blinking and saturation combined with a high contrast provides unique advantages of higher–harmonic generating nanoparticles over fluorescent probes, allowing for prolonged correlation spectroscopy studies. We apply

the coherent intensity fluctuation model derived for spectroscopy analyses to study the mobility of second harmonic generating nanoparticles. A concise protocol is presented for quantifying the diffusion coefficient from a single spectroscopy measurement without the need for separate point–spread–function calibrations. The technique's applicability is illustrated on 55 nm $LiNbO_3$ nanoparticles. We perform label–free raster image correlation spectroscopy imaging in aqueous suspension and spatiotemporal image correlation spectroscopy in A549 human lung carcinoma cells. In good agreement with the expected theoretical result based on the Stokes–Einstein equation, the measured diffusion coefficient in water at room temperature is $(7.5 \pm 0.3)\ \mu m^2/s$. Analyzing the same data set with the expressions for incoherent fluorescence yields $(12 \pm 4)\ \mu m^2/s$. The diffusion coefficient in the cells is more than 10^3 times lower, and heterogeneous, with an average of (3.7 ± 1.5) x $10^{-3}\ \mu m^2/s$.

Keywords

Optical spectroscopy, second harmonic generation, non–linear correlation spectroscopy, spatiotemporal image correlation spectroscopy, raster image correlation spectroscopy

Main text

Fluorescence Correlation Spectroscopy (FCS) has been successfully applied to numerous systems since its first introduction several decades ago.[1,2] In particular, FCS has been used to study the molecular translational and rotational diffusion properties in solutions and in living cells.[3–7] In FCS, quantitative information about the dynamics is derived from the temporal fluorescence intensity fluctuations produced by the randomly moving fluorophores into and out of the diffraction limited volume of a focused illumination beam. Many variations on this principle exist. Scanning FCS (sFCS) allows to measure slower diffusion rates while reducing photobleaching.[8–10] FCS in combination with two–photon

excitation was developed to measure protein aggregation[11] and to probe the mobility of beads in the intracellular transport.[12] In Image Correlation Spectroscopy (ICS), fluctuations in 2D or 3D space are analyzed to quantify the aggregation and the average number of stationary or slowly moving fluorescently labeled structures.[13,14] Both spatial and temporal intensity information can be combined in Raster ICS (RICS)[15–17] and in spatiotemporal ICS (STICS).[18–21] RICS is a variation on sFCS in which the speed of the moving excitation volume in a laser scanning microscope (LSM) is explicitly used to resolve shorter timescale dynamics than covered by STICS. STICS analyzes the spatial and temporal lags in a series of images collected with short acquisition times. This technique not only allows the measurement of the diffusion coefficient, but also mapping flow velocities in a wide dynamic range.

However, fluorescence–based methods carry several disadvantages. Long–term studies of both slow and fast processes are impeded, as fluorophores are sensitive to photobleaching, blinking and saturation.[22–25] In addition, autofluorescence of the environment, which is in particular problematic for imaging in cells and tissues,[26] further complicates the use of fluorescent probes.

These drawbacks are not, or at least a lot less, present in Second Harmonic Generation (SHG) imaging. SHG is a nonlinear scattering process, produced in the bulk of non–centrosymmetric crystal structure materials, such as $BaTiO_3$, $LiNbO_3$, ZnO and $BiFeO_3$.[22,27,28] The second harmonic signal is extremely stable and strong,[22] providing a high contrast in samples that are not SHG active.[29] Harmonic nanoparticles (HNPs), *i.e.* higher–harmonic generating nanoparticles (NPs), are therefore ideal for long–term dynamics studies in complex biological specimens.[22,30–33] Not only can HNPs be employed as optically superior labels, investigating interactions between NPs and human cells is in itself important for *e.g.* nanomaterial safety studies.[19,27]

The coherent nature of SHG requires a different model for analyzing the observed intensity fluctuations. Geissbuehler *et al.* presented the FCS variant with HNPs circulating

through a flow cell, which they termed nonlinear correlation spectroscopy, and derived the corresponding equations for interpreting the data.[23] This model was later extended to a general coherent intensity fluctuation model (cIFM).[34] cIFM describes the intensity correlation between any two points in space and time assuming free diffusion of the particles, with or without flow superimposed. Using for each technique the appropriate substitution, cIFM can be employed for the coherent counterparts of fluorescence–based correlation spectroscopies FCS, TICS, RICS and STICS, which were named coherence Correlation Spectroscopy (cCS), cTICS, cRICS and cSTICS, respectively. The prefix 'c', pronounced as 'coh', stresses the coherent aspect of the scattering process.

Here, we verify cIFM by performing cRICS measurements on SHG active $LiNbO_3$ and $BaTiO_3$ HNPs suspended in water and in a water glycerol mixture. We present a concise protocol for extracting the diffusion coefficient from a single measurement without the need for separate point–spread–function (PSF) calibrations. cSTICS is demonstrated in live adenocarcinomic human alveolar basal epithelial cells (A549 cell line) to illustrate the potential of dynamic SHG correlation spectroscopy measurements in living cells with biocompatible[35] HNPs. Quantitative characterization of the mobility of HNPs within living cells and cell organelles allows to gain insight into the complexity of nanoparticle transport.[32,36]

A typically observed cRICS (56 *nm* $LiNbO_3$ nanoparticles) and fluorescence RICS (100 *nm* beads) frame for comparison are depicted in Fig. 1 and Fig. S1. Note that the spatially summed SHG intensity over time, plotted in Fig. S2, is very stable, due to the absence of bleaching of the HNPs. The combined movement of the $LiNbO_3$ particles and the illumination beam results in a collection of stripes in the images, similarly to what is observed for the fluorescent beads. There is, however, a difference between both images. While the signal from the beads is often detected in multiple consecutive lines, the HNPs show a more discontinuous pattern, in which a particle can be found in one line before disappearing for some time, and then reappearing some lines later. Evidence for

this behavior is provided by the autocorrelation function (ACF) $G(\xi, \psi)$, shown in Fig. 1. The ACF is a function of the spatial lags ξ and ψ in the x and y direction, respectively, which themselves are functions of time in RICS/cRICS because of the scanning motion of the laser beam. The shape of the ACF is affected by both system and sample related parameters. The first class comprises the width ω_0 and height z_0 of the PSF and the Gouy phase shift per unit length κ_q which is present in a focused laser beam.[37] The sample related parameters are the concentration $\langle c \rangle$, diffusion coefficient D and directed flow of the particles $\mathbf{v}$. In the experimental ACF shown in Fig. 1, the central line $G(\xi, \psi = 0)$ protrudes above the rest of the curve, with no effect of the selected scan speed, as indicated in Fig. S3. As a control to exclude sample and system related artifacts, we measured the same sample with a different setup (Fig. S4), and different samples (50 nm $BaTiO_3$ HNPs and 100 nm fluorescent microspheres) with the same setup (Fig. S5–S6). An additional control experiment was performed with immobilized $LiNbO_3$ HNPs (Fig. S7). The fixed HNPs and the fluorescent beads produce a conventional autocorrelation curve, without the central ridge. Although the effect is less pronounced in the water glycerol mixture, all other experiments do show a significant $\psi = 0$ peak, independent of the illumination polarization. Consequently, this behavior must be attributed to the intrinsic movement of the particles. Because the effect is not predicted by the cIFM,[34] it cannot be caused by free translational diffusion of the HNPs. The microsecond range pixel dwell time is much shorter than the expected millisecond range diffusion time for the HNPs, which further confirms the lack of free translational movement at the $\psi = 0$ time scale. A possible explanation for the drop in G from $\psi = 0$ to $\psi = \pm 1$ is rotational diffusion. The SHG signal is sensitive to the orientation of the HNP with respect to the polarization of the incident light, see Fig. 2. This angular dependency was well fitted with a cos^4 function corresponding to a dipole response due to the projection of the c–axis of the HNP on the focal plane. This can be expected for SHG materials belonging to the 3m symmetry class, as has been reported for $BiFeO_3$.[38,39] Even under circularly polarized illumination,

the observed intensity depends on the angle between the induced SHG dipole moment and the sample plane.[40] One could expect to 'lose' part of the correlation from the $\psi = 0$ to the $\psi = \pm 1$ line due to changing orientations of the HNPs during a line scan time. A spherical particle with a diameter of 56 nm suspended in water at room temperature has a characteristic rotational diffusion time, *i.e.* the inverse of the rotational diffusion coefficient, of 137 μs. Except for the slowest scan speed, this value is longer than the pixel dwell time, but significantly shorter than the characteristic translational diffusion time $\omega_0^2/4D$, which is 14.8 ms. An additional motivation for presence of rotational diffusion is presented in Fig. S8, which shows a cRICS stationary line measurement in which a single line, instead of a raster, was repeatedly scanned. The image shows that while some particles are translating slowly and can be observed in dozens of lines, the resulting traces are still discontinuous, showing an on/off pattern in the y direction. This behavior may be explained as rotational diffusion of the HNPs combined with the 'photoselection effect' shown in Fig. 2. It is unlikely that the missing links in the traces can be attributed to axial translational movement of the HNPs out of the focal volume. A more plausible explanation is a change of the orientation of the HNPs in which a lower second harmonic signal is produced. The corresponding ACF shows that the track gaps in the vertical time direction result in a strong decrease in G from the $\psi = 0$ to the $\psi = \pm 1$ line, which leads to the presence of the central ridge.

Although the appearance of a central ridge indicates more complex HNP dynamics than solely translational movement, the absence of noticeable diffusion over several pixel dwell times, even for the slowest scan speeds (Fig. S3), makes the $\psi = 0$ line valuable to obtain an independent calibration of the PSF. Panel (e) of Fig. 1 shows $G(\xi, \psi = 0)$, extracted from the data set from panel (c). The parameters ω_0 and $\langle c \rangle$ were fitted with D fixed at 7 $\mu m^2/s$, but almost identical results were found for $D = 0$. Averaging over 3 measurements at different scan speeds and calculating the standard deviation to determine the confidence intervals yields $\omega_0 = (672 \pm 8)\ nm$ and $\langle c \rangle = (0.47 \pm 0.08)\ /\mu m^3$. An

exemplary fit result is plotted in Fig. 1, panel (e). The concentration corresponds to an average of 1.4 particles in the focal volume, but this number may not be fully reliable due to the central ridge, which is not taken into account in the theoretical model. The size of the PSF, however, is in good agreement with a reference measurement with fixed blue beads excited with the same wavelength. The result after analyzing 17 subresolution 100 nm polystyrene beads is (6.5 ± 0.3) x 10^2 nm.

Fixing the height of the focal volume z_0 is necessary to fit the central autocorrelation line. Based on a z–stack of the blue beads, a shape factor z_0/ω_0 of 5.1 was used throughout this work. It should however be noted that the value of z_0 does not significantly influence the ACF. *E.g.* fixing the z_0/ω_0 ratio at 3 yields a fitted ω_0 value within the aforementioned confidence interval. The minor importance of z_0, combined with the extraction of ω_0 from the central ridge, obviates the need for extra calibration experiments.

The coherent nature of the SHG process affects the shape of the cRICS ACF compared to the fluorescence RICS ACF. The cRICS ACF can be expressed as[34]

$$G = \frac{A3 + A4 + A5 + A7 + B6 + B7 + B9 + C5 + C7}{G_N}, \tag{1}$$

in which all terms in the numerator are functions of the system parameters ω_0, z_0 and κ_q and the sample parameters $\langle c \rangle$ and D. G_N is a normalization factor. The sum $(A7 + B9 + C7)/G_N$ is equal to the fluorescence expression. The contribution of the other terms to G increases with increasing particle concentration. Consequently, when using the fluorescence expression to fit the $\psi = 0$ line, a significantly higher value of (865 ± 4) nm is found for ω_0. This result indicates the importance of using the cIFM for SHG active specimens.

The lateral size of the PSF derived from the central line of the ACF can be employed to calculate the diffusion coefficient from the $\psi \neq 0$ lines. Since the rotational diffusion time is short with respect to the line scan time, the $\psi \neq 0$ are not influenced by rotational diffusion. Fixing all parameters, except $\langle c \rangle$ and D, yields a diffusion coefficient of (7.5 ± 0.3) $\mu m^2/s$,

averaged over four measurements. This result corresponds to the value predicted by the Stokes–Einstein equation, which is $(8 \pm 2)\ \mu m^2/s$ for particles with a diameter between 45.5 nm and 65.5 nm suspended in water at room temperature (viscosity 1.002 $mPa.s$[41]). The quality of the fit is illustrated by the fit residuals of Fig. 3.

A diffusion coefficient of $(12 \pm 4)\ \mu m^2/s$ is found upon analysis of the same data sets with the fluorescence expression and by fixing ω_0 at 672 nm. In addition to substantially overestimating D, the non–random structure of the fit residuals, shown in the central panel of Fig. 3, clearly demonstrates the undesirable quality of this fit result.

The fluorescence model may however be used to examine SHG data if ω_0 is first calculated from the $\psi = 0$ line by means of the fluorescence expression. Even though this method yields a value of $\omega_0 = (865 \pm 4)\ nm$, which does not correspond to the real PSF size, the fitted diffusion coefficient, $(7.6 \pm 0.6)\ \mu m^2/s$, closely matches the result obtained from the cIFM. Furthermore, the quality of the fit is, as illustrated in the right panel of Fig. 3, comparable to the SHG analysis.

One of the main advantages of using SHG active materials for mobility studies is the absence of photobleaching, as illustrated by Fig. S2. Consequently, cSTICS enables long term mapping of the diffusion coefficient in cells, tissues and living organisms. To check the HNP uptake by the cells, we imaged cells that had been exposed to the $LiNbO_3$ HNPs for 24 h, see Fig. S9. The z–stack in the last panel of Fig. S9 shows that the HNPs are really present inside the cell. A cSTICS example is presented in Fig. 4 and Table 1. We analyzed 3 regions inside the cell, which revealed a non–homogeneous diffusion coefficient. The ACF for region 1 is plotted in Fig. S10. No central ridge is observed, which can be attributed to clustering of the HNPs, thereby reducing the SHG intensity dependence on the orientation of the excitation polarization plane. The corresponding diffusion coefficient is 3.8 x $10^{-3}\ \mu m^2/s$, which is several orders of magnitude lower than what is observed in aqueous suspension. Similar values are found for the other regions: the diffusion coefficient and standard deviation averaged over 18 regions spread over 4 cells yields

$D = (3.7 \pm 1.5)$ x 10^{-3} $\mu m^2/s$. Fitting again the data with the fluorescence expression and a PSF width of $\omega_0 = 875$ nm yields an almost identical result with a D value of (3.8 ± 1.8) x 10^{-3} $\mu m^2/s$.

Table 1: Diffusion coefficient heterogeneity for the regions of Fig. 4.

Region	Diffusion coefficient [x 10^{-3} $\mu m^2/s$]
1	3.8
2	6.7
3	2.6

The small diffusion coefficient in comparison to the cRICS result cannot only be explained by clustering of the particles during the 24 hours exposure time, since the cluster diameter would theoretically need to be about 1000 times larger than an individual particle. Instead, the movement of most HNPs must be confined to cellular organelles and the measured diffusion coefficients reflect the mobility of these organelles. The diffusion coefficients we measured are in close proximity to the values found with conventional STICS.[21]

We measured the colocalization of the HNPs with fluorescently labelled lysosomes (N = 7) and endosomes (N = 5), see Fig. S11. The Manders' coefficients were found to be (0.7 ± 0.2) and (0.6 ± 0.2), respectively. These results suggest uptake and clustering of the particles inside both cellular organelles. No directed flow of the HNPs could be found within the accuracy of the cSTICS experiments, indicating the absence of active transport of the organelles. As a second test, we checked specifically for any transport of the organelles via the actin microfilaments and the microtubules by adding latrunculin and nocodazole, respectively, to the cells. Each component changes the polymerization state of the assembly that is affected, thereby severely hindering any transport along these structures.[42,43] Although analysis of 11 regions in 4 cells treated with latrunculin – D = (1.0 ± 1.3) $\mu m^2/s$ – and 15 regions in 4 cells treated with nocodazole – $D = (2.1 \pm 1.6)$ $\mu m^2/s$ – both yield lower diffusion coefficients than untreated cells, the spread in D between different regions

is too large to draw conclusions on the mechanisms involved in the HNP transport.

In summary, we have delineated the cIFM conditions needed to analyze autocorrelation spectroscopy measurements with second harmonic generating light scattering HNPs. The central line from the cRICS autocorrelation curve surprisingly protrudes above the rest of the surface. This central ridge was not predicted by the theory. Analyzing a cRICS data set therefore requires two steps: the central line is fitted separately and is used to extract the beam waist while the diffusion coefficient is obtained from the other lines. No additional PSF calibrations are needed for this type of experiment. The measured diffusion coefficient for 56 *nm* $LiNbO_3$ HNPs suspended in water at room temperature corresponds to the expected value based on the Stokes–Einstein equation. A cSTICS measurement in A549 cells revealed a much lower and heterogeneous mobility, caused by the uptake of the HNPs in cell organelles, such as endosomes and lysosomes. Instead of using the complex cIFM to analyze the ACF, we have shown that for our experiments the fluorescence expression yields the same diffusion coefficient, provided that the beam waist is also measured using the fluorescence model. Further exploration is required to check whether this bypass can be generalized to other systems or samples. Typical challenges with fluorescence RICS and STICS, such as photobleaching and blinking, are absent in higher–harmonic generating materials. Our findings to employ these HNPs for autocorrelation spectroscopy studies will aid specific applications for long term, deep tissue and organoid imaging, tissue engineering, chronic wound-healing and environmental HNPs exposure studies.

Methods

Harmonic nanoparticles

Samples of $BaTiO_3$ HNPs of 50 *nm* were prepared according to the protocol described in Sugiyama *et al.*[44] Phase–pure $LiNbO_3$ HNPs were manufactured according to the protocol described by Mohanty *et al.*[45] and then suspended in deionized water. Measurements

on 200 nm pore filtered $LiNbO_3$ suspensions (Filtropur S 0.2, Sarstedt, Nümbrecht, Germany) with NP tracking analysis (NanoSight NS300, Malvern Panalytical, Almelo, the Netherlands) showed that more than 50 % of the particles have a diameter between 45 nm and 65 nm, with a maximum at 56 nm, see Fig. S12. The particles produce a bright and illumination polarization dependent SHG signal, as illustrated by Fig. 2. Polarization–SHG measurements were performed with a Zeiss LSM 510 META (Carl Zeiss, Jena, Germany) mounted on an Axiovert 200M. A 100 femtosecond 80 MHz pulsed laser (Mai Tai DeepSee, Spectra–Physics Inc., Santa Clara, USA) tuned to a central wavelength of 810 nm with an average power of about 100 mW on the stage (measured with a thermal power sensor S175C, ThorLabs, Dachau/Munich, Germany) was used for two–photon excitation. The near infrared radiation was focused by a Plan–Apochromat 20x/NA 0.75 objective after passing through a homebuilt system containing a rotatable half wave and quarter wave plate. The orientation of the half wave plate was automatically controlled with stepper motors (Trinamic PD–110–42, Hamburg, Germany) to make a series of images with different orientations of the linearly polarized illuminating laser light, see panel (c). The SHG signal was collected in forward mode using a condenser lens. An FT442 nm beam splitter and a narrow band pass filter BP400–410 nm were installed to block the illumination light and to select the SHG signal. For each particle, the pixel values in a small region comprising the particle were summed.

Measurements in suspension

For cRICS measurements, the $LiNbO_3$ and $BaTiO_3$ stock concentrations of 0.5 mg/mL and 1 mg/mL, respectively, were diluted a 100 times in Milli–Q ultrapure water (Merck Millipore, Overijse, Belgium). The suspension was sonicated for 15 minutes in an ultrasound water bath (Elmasonic S 40, 140 W, Elma Schmidbauer GmbH, Singen, Germany) and poured using a syringe through a 200 nm filter (Filtropur S 0.2, Sarstedt, Nümbrecht, Germany). An aliquot of 7 μL was transferred into a well created by mounting a spacer

(Grace Bio–Labs SecureSeal imaging spacer, Sigma–Aldrich, St. Louis, USA, diameter 9 mm, height 0.12 mm) onto a microscope slide. The well was sealed by a cover slip.

cRICS experiments with $LiNbO_3$ were performed at room temperature using a Zeiss LSM 880 (Carl Zeiss, Jena, Germany) mounted on an Axio Observer frame. A Mai Tai DeepSee laser tuned to a central wavelength of 810 nm and with an average power of about 83 mW at the stage was used for two–photon excitation. The laser power was set to the minimum value providing a good signal to noise ratio. The infrared radiation was focused by a Plan–Apochromat 20x/NA 0.8 M27 objective after passing through a homebuilt system containing an automated rotatable half wave and quarter wave plate combination. The orientation of the wave plates was tuned to obtain circularly polarized light at the stage. The SHG signal was collected in backward mode using the same objective. A broad band pass filter LBF 355/690+(R), a short pass dichroic filter FT 442 nm and a narrow band pass filter BP 400-410 nm, respectively, were used to completely block the illumination light and to select the SHG signal. One detector element from the non–descanned BiG.2 detection system was employed in photon counting mode.

Suspension measurements were repeated several times for different scan speeds. A single measurement consisted of a time series of at least 50 frames for the slowest scan speed. To compensate for the lower signal to noise ratio at shorter pixel dwell times, the number of recorded frames was increased for faster scan speeds, resulting in a comparable overall acquisition time, see Table S1 for further experiment detail. At the highest scan speed about 2000 frames are required in a single experiment.

A RICS control experiment was performed with fluorescent carboxylated polystyrene beads (FluoSpheres^{TM}, ex/em 350/440, Invitrogen, Thermo Fisher Scientific, Merelbeke, Belgium) with an average diameter of 100 nm. Before a measurement, the sample was diluted 10,000 times in ultrapure water (Milli–Q) and sonicated for 5 minutes in the aforementioned ultrasound water bath sonicator. The same experimental settings as for cRICS were used, apart from the fluorescence detection, for which a BP450-650 nm filter

was employed, and the average laser power, which was 92 mW.

The cRICS control experiment with $BaTiO_3$ was performed using the same setup as described for the $LiNbO_3$, except for the laser power, which was lowered to 46 mW. An additional control measurement was performed with fixed $LiNbO_3$ HNPs by pouring 7 μL of the $LiNbO_3$ suspension onto a cover slip, waiting until the water has been fully evaporated, and subsequently mounting the cover slip on a microscope slide. A final control measurement consisted of a cRICS experiment in a water glycerol mixture to increase the viscosity of the HNP environment. 100 μL of the HNP suspension was diluted in 900 μL Milli–Q, sonicated for 15 minutes and poured through a 200 nm filter. 291 μL of the resulting sample was added to 2.86 mL glycerol (Sigma–Aldrich, St. Louis, USA) and placed on a hotplate (VMS–A, VWR, Leuven, Belgium) for 30 minutes at about 50 $^{\circ}C$ while continuously mixing with a magnetic stirrer. Then, the sample was 1:2 diluted in Milli–Q and further mixed for several minutes before starting the cRICS measurement.

To rule out possible system dependent artifacts, the cRICS measurement with $LiNbO_3$ HNPs was repeated with the Zeiss LSM 510 META system. Linearly polarized light from the Mai Tai DeepSee laser tuned to a central wavelength of 810 nm with an average power of about 190 mW on the stage was used for two–photon excitation. The infrared radiation was focused by an LD C–Apochomat 40x/NA 1.1 W objective. The SHG signal was collected in backward, non–descanned, analog mode after passing through the same filters as described for the LSM 880.

Measurements in cells

Adenocarcinomic human alveolar basal epithelial cells (A549 cell line, European Collection of Animal Cell Cultures, Wiltshire, UK), were maintained in modified eagle's medium with glutamax (Gibco, Paisley, UK) supplemented with 10 % non–heat inactivated fetal bovine serum (Biochrom AG, Berlin, Germany) and 1 % penicillin/streptomycin (Gibco) at 37 $^{\circ}C$, 5 % CO_2 and 95 % humidity. At $80 - 90$ % confluency, the cells were routinely subcultured

using trypsin–EDTA to detach cells. Two days before the measurement, the cells were plated on Ibidi μ–slide 8 well plate chambers (Ibidi GmbH, Martinsried, Germany) at a density of 15,000 cells/chamber and incubated overnight to allow the cells to adhere. After washing three times with phosphate buffered saline (PBS), cells were treated with HNPs. For this, the stock suspension of $LiNbO_3$ HNPs was diluted 5 times in complete culture medium, filtered through a 200 nm filter and 300 μL/well was added to the plated cells. After 24 h exposure, cells were aspirated and washed three times with PBS before adding complete culture medium for imaging. To study the contribution of cytoskeleton mediated transport, we perturbed two of its most important constituents, actin and tubulin, by adding 0.25 μM latrunculin A (Merck Millipore, Overijse, Belgium) and 20 μM nocodazole (Sigma–Aldrich) in culture medium, respectively. After 30 min of incubation, cells were washed and cSTICS experiments were performed. To check cellular HNP internalization, cells were treated with 12.5 μM CellTracker^{TM} Green CMFDA (Life Technologies, Merelbeke, Belgium) for 45 minutes in serum free cell culture medium and thereafter washed three times with PBS. For the HNP internalization experiment, a z–stack was acquired with a total volume of 180 x 180 x 20 μm^3 comprising 20 images and a step size of 841 nm. The cellular lysosomes and endosomes were stained using 1 μM LysoTracker Green DND–26 (30 minutes, Molecular Probes, Thermo Fisher Scientific, Merelbeke, Belgium) and CellLight Endosomes–GFP, BacMama 2.0 (16 h, 200000 particles, Thermo Fisher Scientific, Germany), respectively. SHG and fluorescence were simultaneously imaged in descanned mode. The second harmonic signal was generated with the Mai Tai DeepSee at 810 nm and detected in the BP400–410 nm channel, while the fluorescence was excited with an Ar–ion laser at 488 nm and detected in the BP500–550 nm channel. Manders overlap coefficients, describing the fraction of HNPs that are associated with the labelled cell organelles, were calculated using the Fiji plugin JACoP (ImageJ 1.52c, open source software, http://fiji.sc/Fiji). A threshold was set to the approximated background value prior to the analysis. Note that coefficients are not dependent on the intensities of each

channel and cross–talk between the different imaging channels was found to be negligible.

cSTICS experiments were executed with linearly polarized light with an average biocompatible laser power[46] of about 16 mW at the sample position. Cells were kept at 37 $^{\circ}C$ and 5 % CO_2 during the experiments by means of a stage incubator. The acquisition time of each frame was about 5 s and 200 frames were recorded in total.

Data analysis

Data analysis was performed according to our expressions derived in Slenders *et al.*[34] with custom written scripts in Matlab (Matlab R2017b, The Mathworks Inc., Eindhoven, The Netherlands). The ACF $G(\xi, \psi)$ is a function of the spatial lags ξ and ψ in the x and y direction, respectively, which themselves are functions of time in cRICS. The parameters affecting the ACF shape are the PSF of the system, and the concentration, diffusion coefficient and directed flow of the particles.

For cRICS, the ACF G of all frames was calculated using fast Fourier transforms. The series was subsequently ordered from the best to the worst autocorrelation curve by means of an adaptation of the spike cluster filtering algorithm presented by Ries *et al.*[47] Details of the protocol can be found in the SI. The 25 % best autocorrelation curves were averaged, and the inverse of the square root of the variance was used as the fit weights in a nonlinear least squares approach. For representation purposes, the $G(0,0)$ noise peak was removed from the surface plots by setting this value to $G(1,0)$. The central line of the ACF in the scan direction ($\psi = 0$) was fitted separately from the other lines to extract ω_0, *i.e.* the lateral size ($1/e^4$ value) of the PSF. Apart from ω_0, two other unknowns are the average particle concentration $\langle c \rangle$ and the phase shift per unit length κ_q which is present in a focused laser beam.[37] The variable $\langle c \rangle$ was left as a second fit parameter. Slenders *et al.* showed however, that when κ_q is also left as a free parameter, the fit process becomes unstable.[34] We therefore estimated this variable *a priori* by performing the central line fit with ω_0 and $\langle c \rangle$ as the only freely adjusting parameters and we subsequently computed a new κ_q based on the

outcome. This process was iteratively repeated until the resulting value for the phase factor fluctuated less than 0.1 %. κ_q is a parameter describing a linear approximation to the real Gouy phase shift and was calculated in each iteration as $\lambda/(\pi\omega_0^2)$, with λ the illumination wavelength. Although a value of $2\lambda/(\pi\omega_0^2)$ is theoretically a better estimate of κ_q near the focal plane for SHG imaging, the true phase shift would be severely overestimated near the top and bottom of the focal volume and the iteration process does not converge. The lines $\psi \neq 0$ were subsequently fitted with the resulting ω_0 value fixed and the diffusion coefficient D and $\langle c \rangle$ as free parameters.

The cSTICS analysis was performed similarly, except for two adjustments. Firstly, the immobile fraction was removed before the calculation of the ACF by subtracting the average image from each frame. The mean value of the average image was then added to all frames to keep the overall amount of photon counts constant. Secondly, the mobility was probed locally by considering specific regions of 64x64 pixels, rather than analyzing the full field–of–view.[48]

Confidence intervals for all experiments were computed as the standard deviation of a set of measurements. Scripts may be made available upon contacting the authors.

Acknowledgement

This research was supported by the Research Foundation Flanders (Fonds Wetenschappelijk Onderzoek, project G092915FWO) and by the Interuniversity Attraction Poles Program (IAP FS2 P7/05, Functional Supramolecular Systems) initiated by the Belgian Science Policy Office. The authors are grateful to prof. dr. J. D'Haen for the SEM image, to dr. N. Smisdom for the fruitful discussions and to dr. R. Paesen and dr. N. Smisdom for the design of the polarization unit. Research in P.P. laboratory was supported by the Office of Science, Office of Basic Energy Sciences, of the U.S. Department of Energy under Contract No. DE–AC02–05CH11231. P.P. declares competing financial interests. Aspects of the work

mentioned in this work are the subject of granted patents and patent applications filed by the Swiss Federal Institute of Technology in Zurich (ETH Zurich), Zurich, Switzerland and the California Institute of Technology (Caltech), Pasadena, CA, USA.

Supporting Information Available

The following files are available free of charge.

- Slenders_et_al_SI.pdf: this document contains additional figures, the autocorrelation sorting protocol and a table with the instrumental settings used in the cRICS measurements.

References

(1) Magde, D.; Webb, W. W.; Elson, E. Thermodynamic fluctuations in a reacting system - measurement by fluorescence correlation spectroscopy. *Physical Review Letters* **1972**, *29*, 705–708.

(2) Elson, E. L.; Magde, D. Fluorescence correlation spectroscopy. I. Conceptual basis and theory. *Biopolymers* **1974**, *13*, 1–27.

(3) Rigler, R.; Grasselli, P.; Ehrenberg, M. Fluorescence correlation spectroscopy and application to the study of Brownian-motion of biopolymers. *Phys. Scr.* **1979**, *19*, 486–490.

(4) Palmer, A. G.; Thompson, N. L. Molecular aggregation characterized by high-order autocorrelation in fluorescence correlation spectroscopy. *Biophys. J.* **1987**, *52*, 257–270.

(5) Kask, P.; Piksarv, P.; Mets, U.; Pooga, M.; Lippmaa, E. Fluorescence correlation spectroscopy in the nanosecond time range - rotational diffusion of bovine carbonic anhydrase-B. *Eur. Biophys. J. Biophys. Lett.* **1987**, *14*, 257–261.

(6) Schwille, P.; Korlach, J.; Webb, W. W. Fluorescence correlation spectroscopy with single-molecule sensitivity on cell and model membranes. *Cytometry* **1999**, *36*, 176–182.

(7) Brock, R.; Hink, M. A.; Jovin, T. M. Fluorescence correlation microscopy of cells in the presence of autofluorescence. *Biophys. J.* **1998**, *75*, 2547–2557.

(8) Weissman, M.; Schindler, H.; Feher, G. Determination of molecular-weights by fluctuation spectroscopy - application to DNA. *P. Natl. Acad. Sci. USA* **1976**, *73*, 2776–2780.

(9) Petersen, N. O. Scanning fluorescence correlation spectroscopy 1. Theory and simulation of aggregation measurements. *Biophys. J.* **1986**, *49*, 809–815.

(10) Ruan, Q. Q.; Cheng, M. A.; Levi, M.; Gratton, E.; Mantulin, W. W. Spatial-temporal studies of membrane dynamics: Scanning fluorescence correlation spectroscopy (SFCS). *Biophys. J.* **2004**, *87*, 1260–1267.

(11) Berland, K. M.; So, P. T. C.; Chen, Y.; Mantulin, W. W.; Gratton, E. Scanning two-photon fluctuation correlation spectroscopy: Particle counting measurements for detection of molecular aggregation. *Biophys. J.* **1996**, *71*, 410–420.

(12) Berland, K. M.; So, P. T. C.; Gratton, E. 2-photon fluorescence correlation spectroscopy - method and application to the intracellular environment. *Biophys. J.* **1995**, *68*, 694–701.

(13) Petersen, N. O.; Hoddelius, P. L.; Wiseman, P. W.; Seger, O.; Magnusson, K. E. Quantitation of membrane-receptor distributions by image correlation spectroscopy - concept and application. *Biophys. J.* **1993**, *65*, 1135–1146.

(14) Kolin, D. L.; Wiseman, P. W. Advances in image correlation spectroscopy: Measuring number densities, aggregation states, and dynamics of fluorescently labeled macromolecules in cells. *Cell Biochem. Biophys.* **2007**, *49*, 141–164.

(15) Digman, M. A.; Sengupta, P.; Wiseman, P. W.; Brown, C. M.; Horwitz, A. R.; Gratton, E. Fluctuation correlation spectroscopy with a laser-scanning microscope: Exploiting the hidden time structure. *Biophys. J.* **2005**, *88*, L33–L36.

(16) Rossow, M. J.; Sasaki, J. M.; Digman, M. A.; Gratton, E. Raster image correlation spectroscopy in live cells. *Nat. Protoc.* **2010**, *5*, 1761–1774.

(17) Digman, M. A.; Gratton, E. Analysis of Diffusion and Binding in Cells Using the RICS Approach. *Microsc. Res. Tech.* **2009**, *72*, 323–332.

(18) Hebert, B.; Costantino, S.; Wiseman, P. W. Spatiotemporal image correlation Spectroscopy (STICS) theory, verification, and application to protein velocity mapping in living CHO cells. *Biophys. J.* **2005**, *88*, 3601–3614.

(19) Schumann, C.; Schubbe, S.; Cavelius, C.; Kraegeloh, A. A correlative approach at characterizing nanoparticle mobility and interactions after cellular uptake. *J. Biophotonics* **2012**, *5*, 117–127.

(20) Wiseman, P. W. Image correlation spectroscopy: mapping correlations in space, time, and reciprocal space. *Methods Enzymol.* **2013**, *518*, 245–267.

(21) Deville, S.; Penjweini, R.; Smisdom, N.; Notelaers, K.; Nelissen, I.; Hooyberghs, J.; Ameloot, M. Intracellular dynamics and fate of polystyrene nanoparticles in A549 Lung epithelial cells monitored by image (cross-) correlation spectroscopy and single particle tracking. *Biochim. Biophys. Acta, Mol. Cell Res.* **2015**, *1853*, 2411–2419.

(22) Pantazis, P.; Maloney, J.; Wu, D.; Fraser, S. E. Second harmonic generating (SHG) nanoprobes for in vivo imaging. *P. Natl. Acad. Sci. USA* **2010**, *107*, 14535–14540.

(23) Geissbuehler, M.; Bonacina, L.; Shcheslavskiy, V.; Bocchio, N. L.; Geissbuehler, S.; Leutenegger, M.; Marki, I.; Wolf, J. P.; Lasser, T. Nonlinear Correlation Spectroscopy (NLCS). *Nano Lett.* **2012**, *12*, 1668–1672.

(24) Dempsey, W. P.; Fraser, S. E.; Pantazis, P. SHG nanoprobes: Advancing harmonic imaging in biology. *BioEssays* **2012**, *34*, 351–360.

(25) Broillet, S.; Sato, A.; Geissbuehler, S.; Pache, C.; Bouwens, A.; Lasser, T.; Leutenegger, M. Optical coherence correlation spectroscopy (OCCS). *Opt. Express* **2014**, *22*, 782–802.

(26) Roederer, M.; Murphy, R. F. Cell-by-cell autofluorescence correction for low signal-to-noise systems - application to epidermal growth-factor endocytosis by 3T3 fibroblasts. *Cytometry* **1986**, *7*, 558–565.

(27) Staedler, D. et al. Harmonic Nanocrystals for Biolabeling: A Survey of Optical Properties and Biocompatibility. *ACS Nano* **2012**, *6*, 2542–2549.

(28) Clarke, G.; Rogov, A.; McCarthy, S.; Bonacina, L.; Gun'ko, Y.; Galez, C.; Le Dantec, R.; Volkov, Y.; Mugnier, Y.; Prina-Mello, A. Preparation from a revisited wet chemical route of phase-pure, monocrystalline and SHG-efficient BiFeO3 nanoparticles for harmonic bio-imaging. *Sci. Rep.* **2018**, *8*, 10473.

(29) Culic-Viskota, J.; Dempsey, W. P.; Fraser, S. E.; Pantazis, P. Surface functionalization of barium titanate SHG nanoprobes for in vivo imaging in zebrafish. *Nat. Protoc.* **2012**, *7*, 1618–1633.

(30) Grange, R.; Lanvin, T.; Hsieh, C. L.; Pu, Y.; Psaltis, D. Imaging with second-harmonic radiation probes in living tissue. *Biomedical Optics Express* **2011**, *2*, 2532–2539.

(31) Bonacina, L. Nonlinear Nanomedecine: Harmonic Nanoparticles toward Targeted Diagnosis and Therapy. *Mol. Pharmaceutics* **2013**, *10*, 783–792.

(32) Macias-Romero, C.; Didier, M. E. P.; Zubkovs, V.; Delannoy, L.; Dutto, F.; Radenovic, A.; Roke, S. Probing Rotational and Translational Diffusion of Nanodoublers in Living Cells on Microsecond Time Scales. *Nano Lett.* **2014**, *14*, 2552–2557.

(33) Dubreil, L.; Leroux, I.; Ledevin, M.; Schleder, C.; Lagalice, L.; Lovo, C.; Fleurisson, R.; Passemard, S.; Kilin, V.; Gerber-Lemaire, S.; Colle, M. A.; Bonacina, L.; Rouger, K. Multi-harmonic Imaging in the Second Near-Infrared Window of Nanoparticle-Labeled Stem Cells as a Monitoring Tool in Tissue Depth. *ACS Nano* **2017**, *11*, 6672–6681.

(34) Slenders, E.; vandeVen, M.; Hooyberghs, J.; Ameloot, M. Coherent intensity fluctuation model for autocorrelation imaging spectroscopy with higher harmonic generating point scatterers-a comprehensive theoretical study. *Phys. Chem. Chem. Phys.* **2015**, *17*, 18937–18943.

(35) Li, J. H.; Qiu, J. C.; Guo, W. B.; Wang, S.; Ma, B. J.; Mou, X. N.; Tanes, M.; Jiang, H. D.; Liu, H. Cellular internalization of LiNbO3 nanocrystals for second harmonic imaging and the effects on stem cell differentiation. *Nanoscale* **2016**, *8*, 7416–7422.

(36) Panariti, A.; Miserocchi, G.; Rivolta, I. The effect of nanoparticle uptake on cellular behavior: disrupting or enabling functions? *Nanotechnol., Sci. Appl.* **2012**, *5*, 87–100.

(37) Feng, S. M.; Winful, H. G. Physical origin of the Gouy phase shift. *Opt. Lett.* **2001**, *26*, 485–487.

(38) Schmidt, C.; Riporto, J.; Uldry, A.; Rogov, A.; Mugnier, Y.; Le Dantec, R.; Wolf, J. P.; Bonacina, L. Multi-Order Investigation of the Nonlinear Susceptibility Tensors of Individual Nanoparticles. *Sci. Rep.* **2016**, *6*, 9.

(39) Riporto, J.; Demierre, A.; Kilin, V.; Balciunas, T.; Schmidt, C.; Campargue, G.; Urbain, M.; Baltuska, A.; Le Dantec, R.; Wolf, J. P.; Mugnier, Y.; Bonacina, L. Bismuth ferrite dielectric nanoparticles excited at telecom wavelengths as multicolor sources by second, third, and fourth harmonic generation. *Nanoscale* **2018**, *10*, 8146–8152.

(40) Hsieh, C. L.; Pu, Y.; Grange, R.; Psaltis, D. Second harmonic generation from nanocrys-

tals under linearly and circularly polarized excitations. *Opt. Express* **2010**, *18*, 11917–11932.

(41) Lide, D. R. *CRC Handbook of Chemistry and Physics*; CRC Press, 2005.

(42) Coue, M.; Brenner, S. L.; Spector, I.; Korn, E. D. Inhibition of actin polymerization by latrunculin-A. *FEBS Lett.* **1987**, *213*, 316–318.

(43) Kulkarni, R. P.; Wu, D. D.; Davis, M. E.; Fraser, S. E. Quantitating intracellular transport of polyplexes by spatio-temporal image correlation spectroscopy. *P. Natl. Acad. Sci. USA* **2005**, *102*, 7523–7528.

(44) Sugiyama, N.; Sonay, A. Y.; Tussiwand, R.; Cohen, B. E.; Pantazis, P. Effective Labeling of Primary Somatic Stem Cells with BaTiO3 Nanocrystals for Second Harmonic Generation Imaging. *Small* **2018**, *14*, 9.

(45) Mohanty, D.; Chaubey, G. S.; Yourdkhani, A.; Adireddy, S.; Caruntu, G.; Wiley, J. B. Synthesis and piezoelectric response of cubic and spherical LiNbO3 nanocrystals. *RSC Adv.* **2012**, *2*, 1913–1916.

(46) Bove, H.; Steuwe, C.; Fron, E.; Slenders, E.; D'Haen, J.; Fujita, Y.; Uji-i, H.; vandeVen, M.; Roeffaers, M.; Ameloot, M. Biocompatible Label-Free Detection of Carbon Black Particles by Femtosecond Pulsed Laser Microscopy. *Nano Lett.* **2016**, *16*, 3173–3178.

(47) Ries, J.; Bayer, M.; Csucs, G.; Dirkx, R.; Solimena, M.; Ewers, H.; Schwille, P. Automated suppression of sample-related artifacts in Fluorescence Correlation Spectroscopy. *Opt. Express* **2010**, *18*, 11073–11082.

(48) Gielen, E.; Smisdom, N.; vandeVen, M.; De Clercq, B.; Gratton, E.; Digman, M.; Rigo, J. M.; Hofkens, J.; Engelborghs, Y.; Ameloot, M. Measuring Diffusion of Lipid-like Probes in Artificial and Natural Membranes by Raster Image Correlation Spec-

troscopy (RICS): Use of a Commercial Laser-Scanning Microscope with Analog Detection. *Langmuir* **2009**, *25*, 5209–5218.

Graphical TOC Entry

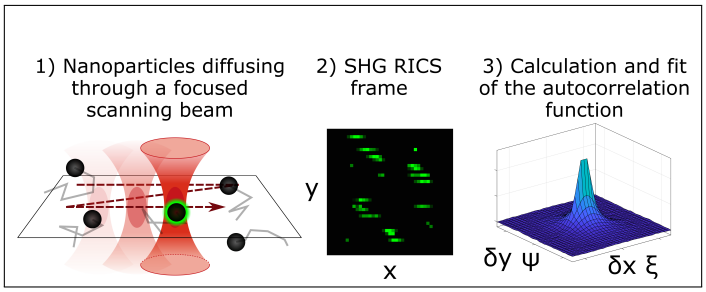

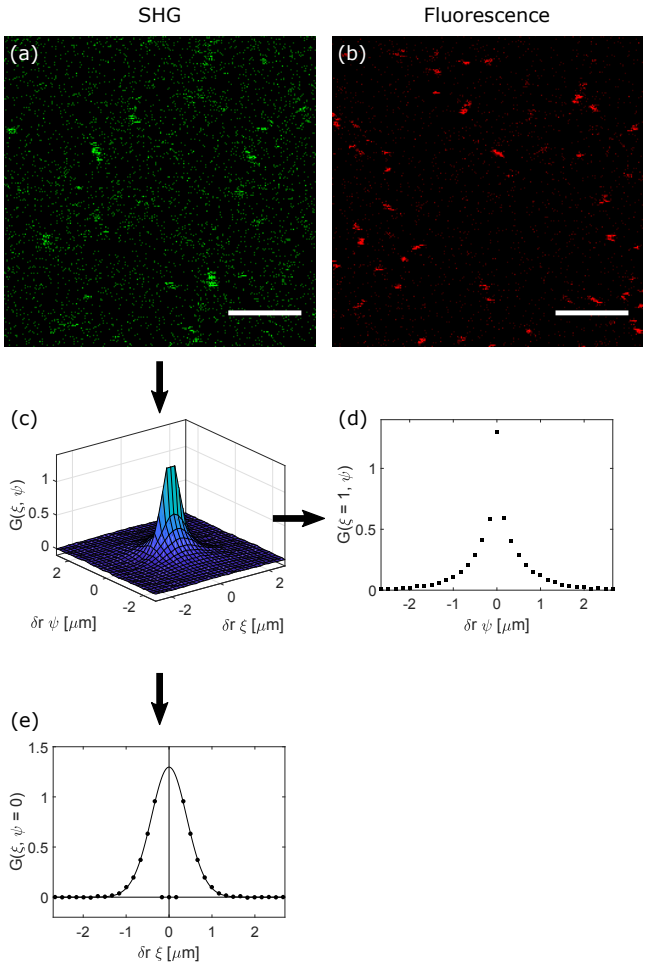

Figure 1: (a) cRICS frame with $LiNbO_3$ HNPs suspended in water at room temperature. Experimental settings: pixel size $\delta r = 166\ nm$, 256x256 pixels, pixel dwell time 8.19 μs, 20x/NA 0.8 objective, Mai Tai at 810 nm, 83 mW on the stage, circularly polarized light, sample at room temperature. SHG detection in the BP400–410 nm channel. (b) RICS frame with 100 nm blue fluorescent carboxylated microspheres. Laser power 70 mW on the stage. Fluorescence detection in the BP450–650 nm channel. All other experimental settings identical to panel (a). Scale bars 10 μm. (c) cRICS autocorrelation curve. From the time series of 800 frames, the 200 best autocorrelation curves were averaged. (d) $G(\xi = 1, \psi)$ cross–section. The cross–section $G(\xi = 0, \psi)$ cannot be used to illustrate the central ridge due to the noise peak at $G(\xi = 0, \psi = 0)$. (e) $G(\xi, \psi = 0)$ cross–section, with the three central points omitted, and fit. The fitted parameter values are the PSF width $\omega_0 = 676\ nm$ and the average particle concentration $\langle c \rangle = 0.41\ /\mu m^3$.

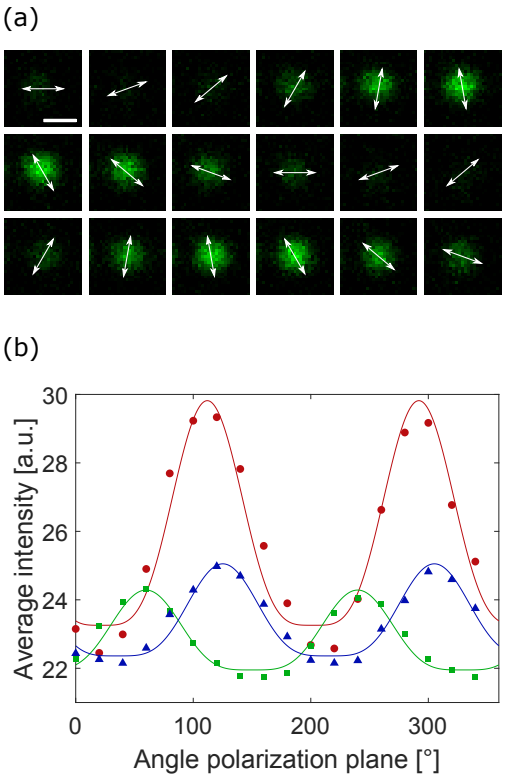

Figure 2: (a) Illustration of the SHG intensity as a function of the orientation of the illumination polarization plane for fixed $LiNbO_3$ HNPs. The second harmonic signal generated by the HNP is brightest when the polarization plane of the incident light is aligned with the dipole moment induced in the HNP. Almost no SHG is detected when the illumination polarization plane is rotated over 90 °. Scale bar 1 μm. (b) Illustration of the $LiNbO_3$ SHG intensity as a function of the orientation of the illumination polarization plane for three spots, indicated with the different colors. The polarization plane was rotated in steps of 20 °. Angles are defined as counterclockwise rotations with the zero angle being along the horizontal. The continuous lines show the cos^4 fits.

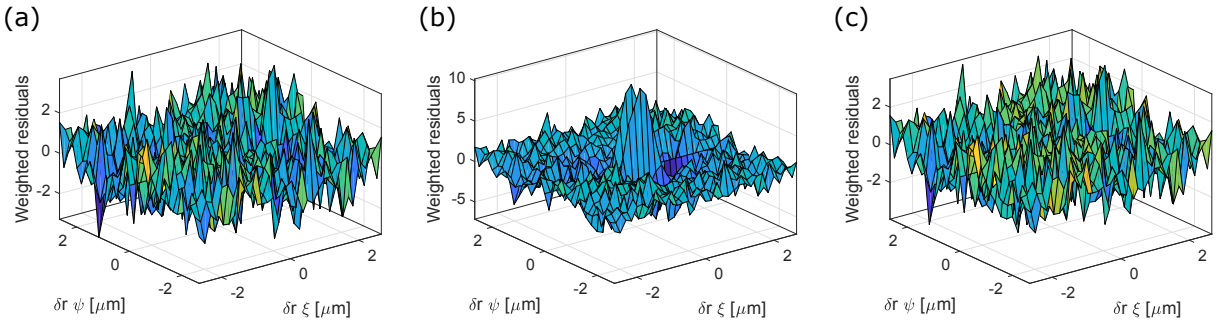

Figure 3: $LiNbO_3$ cRICS fit residuals from the ACFs from Fig. 1 using (a) the cIFM with the PSF width ω_0 fixed at 672 nm and (b–c) using the fluorescence model with (b) $\omega_0 = 672\ nm$ and with (c) $\omega_0 = 865\ nm$. The corresponding diffusion coefficients averaged over 4 measurements are $(7.5 \pm 0.3)\ \mu m^2/s$, $(12 \pm 4)\ \mu m^2/s$ and $(7.6 \pm 0.6)\ \mu m^2/s$. The reduced χ^2 values are 1.3, 3.3 and 1.5, respectively.

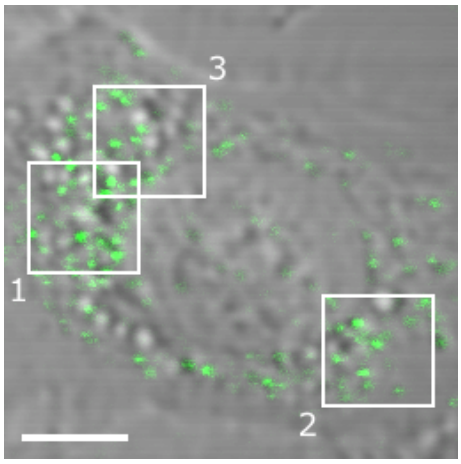

Figure 4: cSTICS measurement of $LiNbO_3$ HNPs (green) in an A549 cell (transmission image). See Table 1 for the measured diffusion coefficients of the different regions. Scale bar 10 μm.

Supporting Information: Image Correlation Spectroscopy with Second Harmonic Generating nanoparticles in suspension and in cells

Eli Slenders,[†] Hannelore Bové,[†] Mathias Urbain,[‡] Yannick Mugnier,[‡] Ali Yasin Sonay,[¶] Periklis Pantazis,[¶] Luigi Bonacina,[§] Pieter Vanden Berghe,[‖] Martin vandeVen,[†] and Marcel Ameloot*,[†]

†*Biomedical Research Institute (BIOMED), Hasselt University, Agoralaan Bldg. C, 3590 Diepenbeek, Belgium*

‡*Univ. Savoie Mont Blanc, SYMME, F–74000, Annecy, France*

¶*Department of Biosystems Science and Engineering, ETH Zürich, Mattenstrasse 26, 4058 Basel, Switzerland*

§*Department of Applied Physics, Université de Genève, Chemin de Pinchat 22, Geneva, Switzerland*

‖*Laboratory for Enteric Neuroscience (LENS), TARGID, University of Leuven, Herestraat 49, 3000 Leuven, Belgium*

E-mail: marcel.ameloot@uhasselt.be

Phone: +32 (0)11 26 92 33. Fax: +32 (0)11 26 92 99

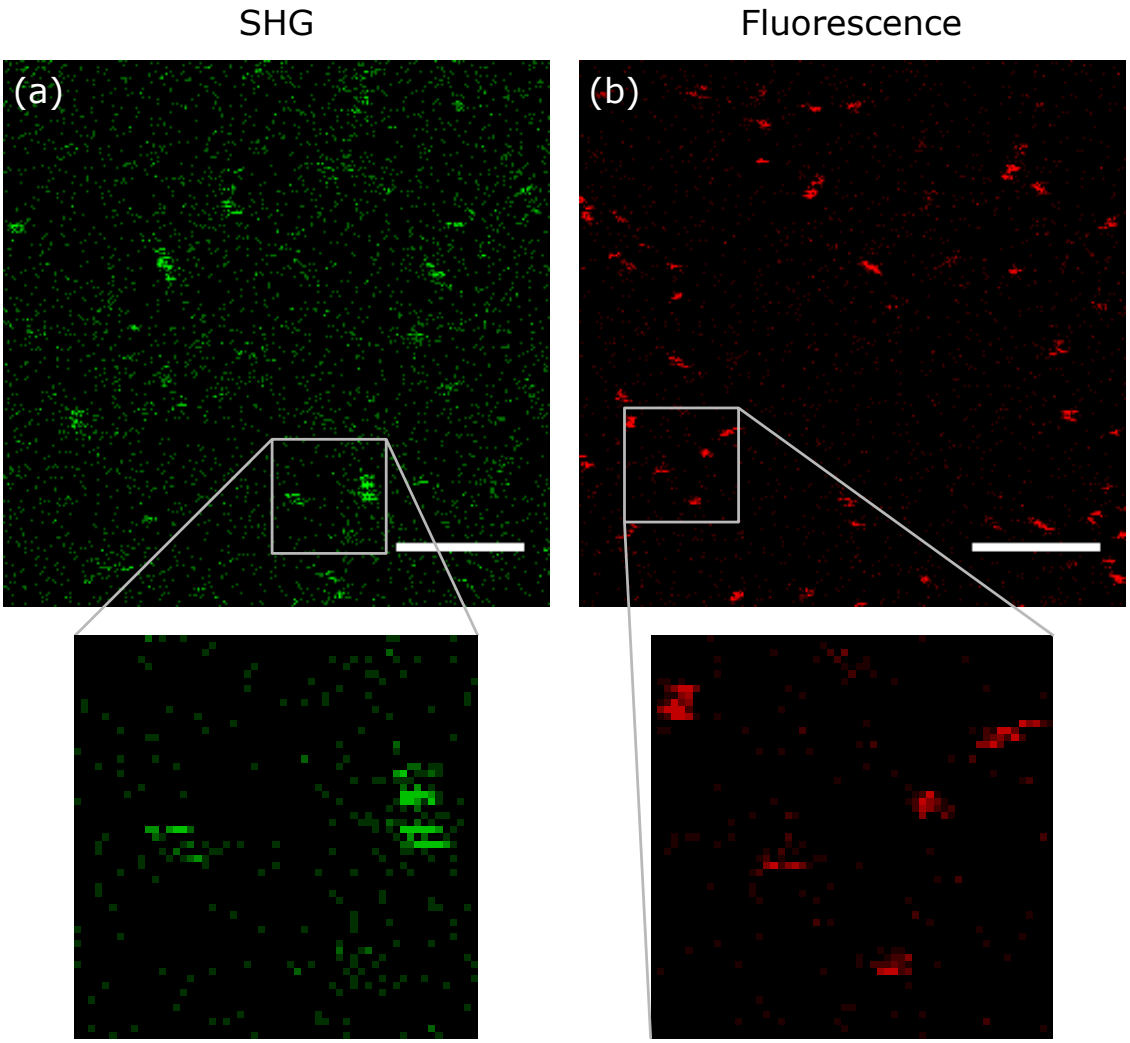

Figure S1: (a) cRICS frame with $LiNbO_3$ HNPs suspended in water at room temperature. (b) RICS frame with 100 *nm* blue fluorescent carboxylated microspheres. The large panels are identical to Fig. 1, main text. The zoomed regions show the difference between the SHG and the fluorescence pattern. When a fluorescent bead is detected, the signal is usually detected in multiple consecutive lines. In contrast, in the SHG image, the pattern is often discontinuous in the y direction.

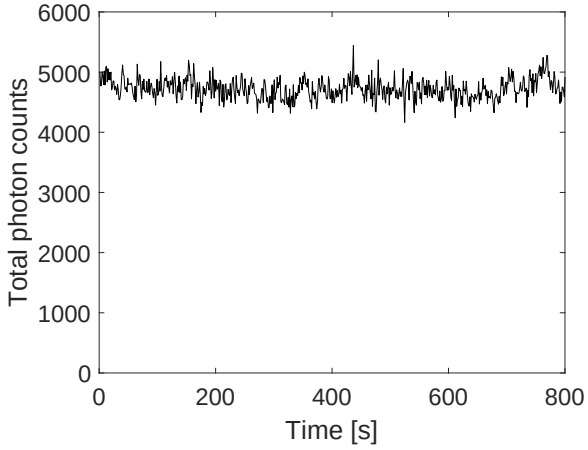

Figure S2: Summed SHG intensity for each frame as a function of the exposure time for cRICS measurement 6, see Table S1 for experimental details.

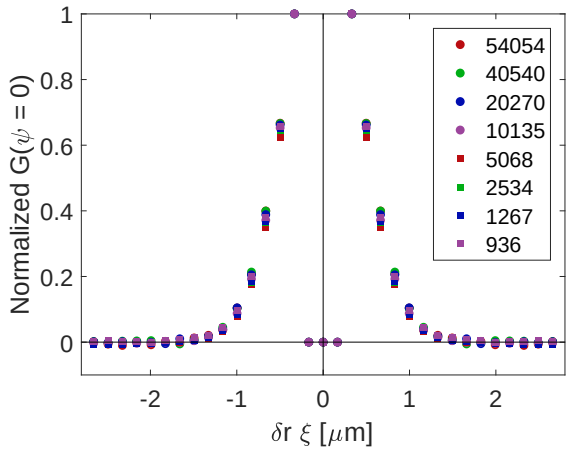

Figure S3: Plots of the normalized central autocorrelation line $G(\xi, \psi = 0)$ for $LiNbO_3$ in water at room temperature at different scan speeds, see the legend, in $\mu m/s$. For each curve, the central data point and its nearest neighbors are set to zero. An overview of the corresponding instrumental parameters is presented in Table S1. No effect of the scan speed is observed, indicating that the particles are not significantly moving during the time the particles reside inside the focal volume, not even for the slowest scan speeds. The observed correlation is therefore a direct consequence of the PSF size.

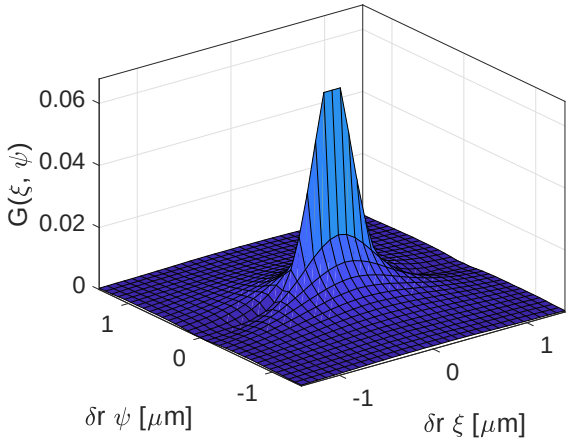

Figure S4: ACF of $LiNbO_3$ NPs in ultrapure Milli–Q water at room temperature, measured with a Zeiss LSM 510 META. Measurement settings: pixel size 88 nm, 512x512 pixels per image, pixel dwell time 6.40 μs, time series of 200 images, 40x/NA 1.1 W objective. Mai Tai laser at 810 nm, 180 mW on the stage, linearly polarized along the horizontal scan direction. Detection in backward, non–descanned mode in the BP400–410 nm channel.

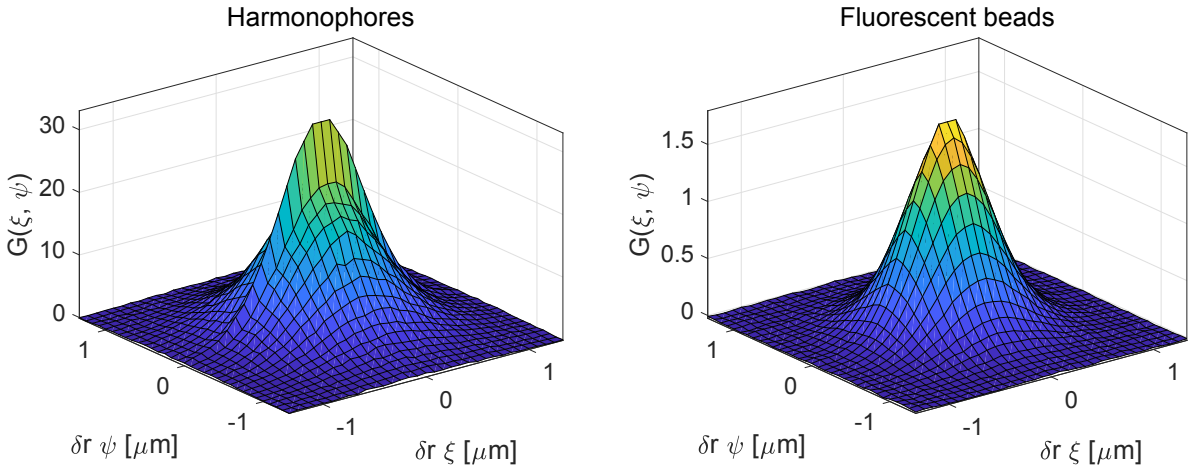

Figure S5: Comparison of the cRICS ACF for (left) 50 nm $BaTiO_3$ NPs and (right) the RICS ACF for 100 nm blue fluorescent carboxylate–modified microspheres (ex/em 350/440) in ultrapure Milli–Q water. The central ridge is only observed for the HNPs. Settings: pixel dwell time 0.67 μs, pixel size 83 nm, 256 x 256 pixels, time series of 1000 frames, laser wavelength 810 nm, power on the stage 46 mW (HNPs) and 92 mW (fluorescent beads), circularly polarized excitation light, samples at room temperature.

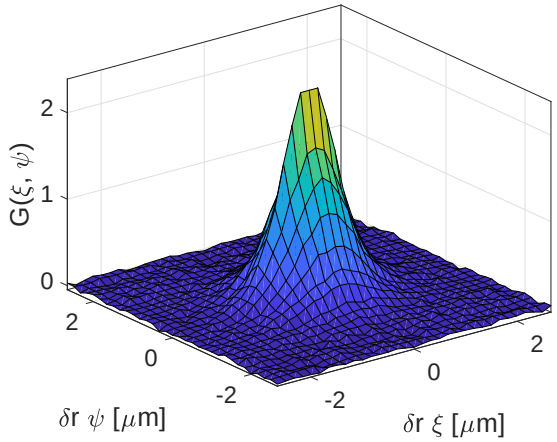

Figure S6: cRICS ACF for $LiNbO_3$ NPs in the water glycerol mixture at room temperature. Illumination at 810 nm with about 105 mW of circularly polarized laser light on the stage. Pixel size 166 nm, pixel dwell time 32.8 μs, 256 x 256 pixels per frame, 75 frames, 20x/NA 0.8 objective. The central ridge is visible, but less pronounced compared to the HNPs in less viscous medium from Fig. S4.

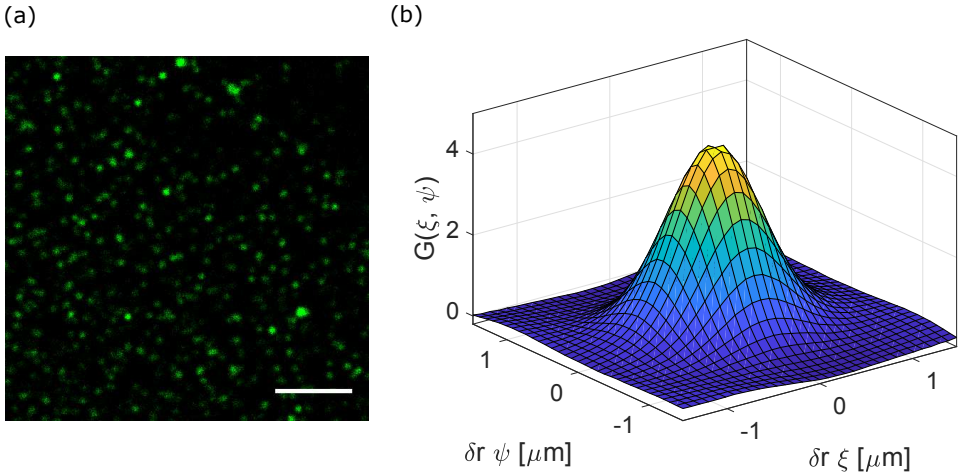

Figure S7: (a) SHG image from dried $LiNbO_3$ NPs. Illumination at 810 nm with about 17 mW of linearly polarized laser light on the stage. Pixel size 92 nm, pixel dwell time 4.10 μs, 512 x 512 pixels, 20x/NA 0.8 objective. (b) Corresponding ACF. No central ridge is observed for fixed particles. Scale bar 10 μm.

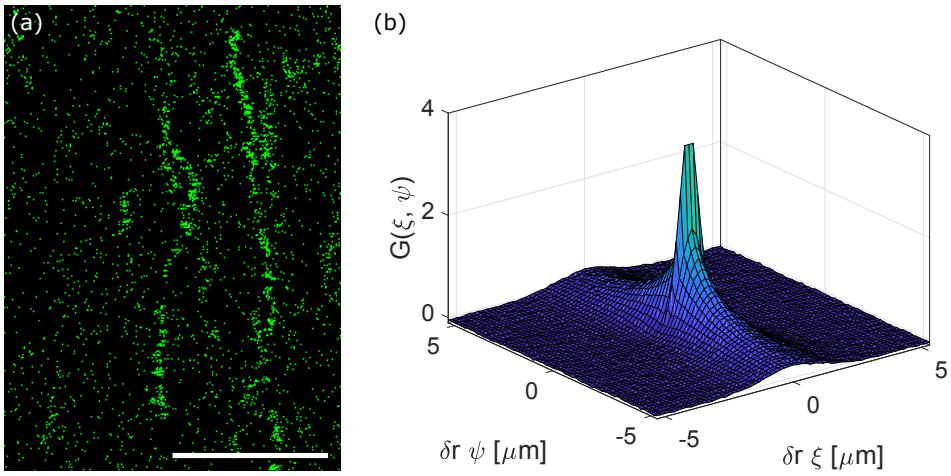

Figure S8: (a) Carpet plot of part of a line scan cRICS measurement with $LiNbO_3$ NPs in ultrapure Milli–Q water at room temperature. The same 42.50 μm horizontal line segment was scanned a total amount of 64000 times. The resulting line signals were plotted below each other, creating the illusion of flow in the y–direction. Scale bar 20 μm. Pixel size 166 nm, 256 pixels per line, pixel dwell time 4.10 μs, 20x/NA 0.8 objective. Illumination at 810 nm with about 83 mW of circularly polarized light on the stage. (b) Corresponding ACF, calculated by splitting the carpet in non–overlapping images of 256 x 256 pixels and applying the same filtering algorithm as in conventional cRICS measurements on the resulting series.

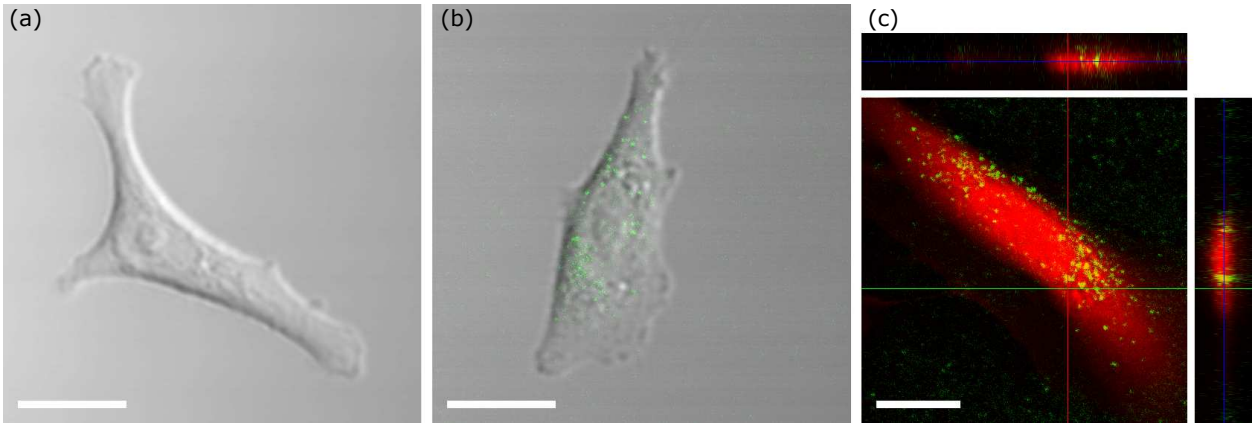

Figure S9: (a) Transmission image of an A549 cell not exposed to NPs. (b) A549 exposed for 24 hours to $LiNbO_3$ NPs (green). (c) z stack with xz and yz cross sections of a CellTracker^{TM} labelled A549 cell (red) exposed to $LiNbO_3$ NPs (green). All observations are at 37 $^{\circ}C$. Scale bars 20 μm.

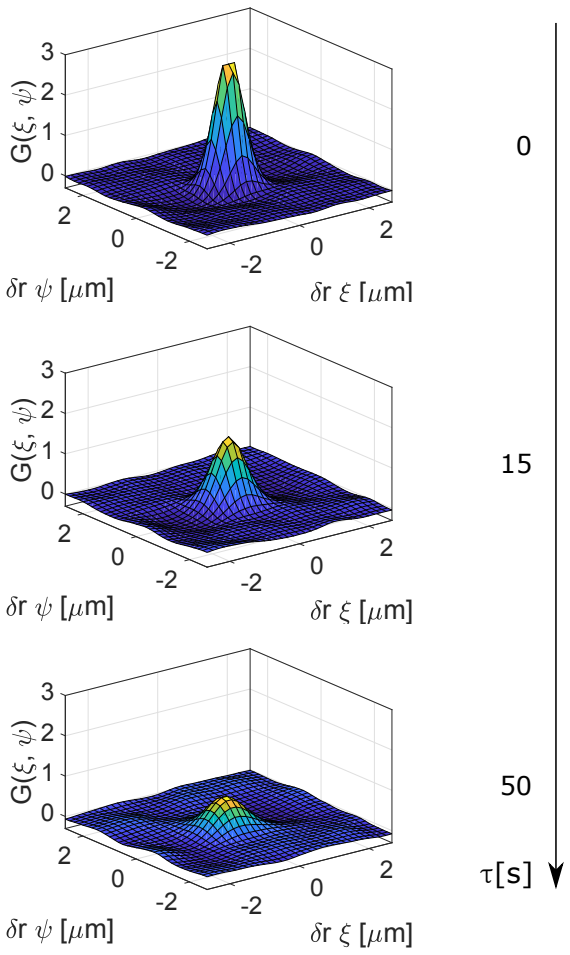

Figure S10: cSTICS ACF for region 1 of Fig. 4 for several lag times in an A549 cell at 37 °C, yielding a D value of 3.8 x 10^{-3} $\mu m^2/s$. Note the absence of the central ridge.

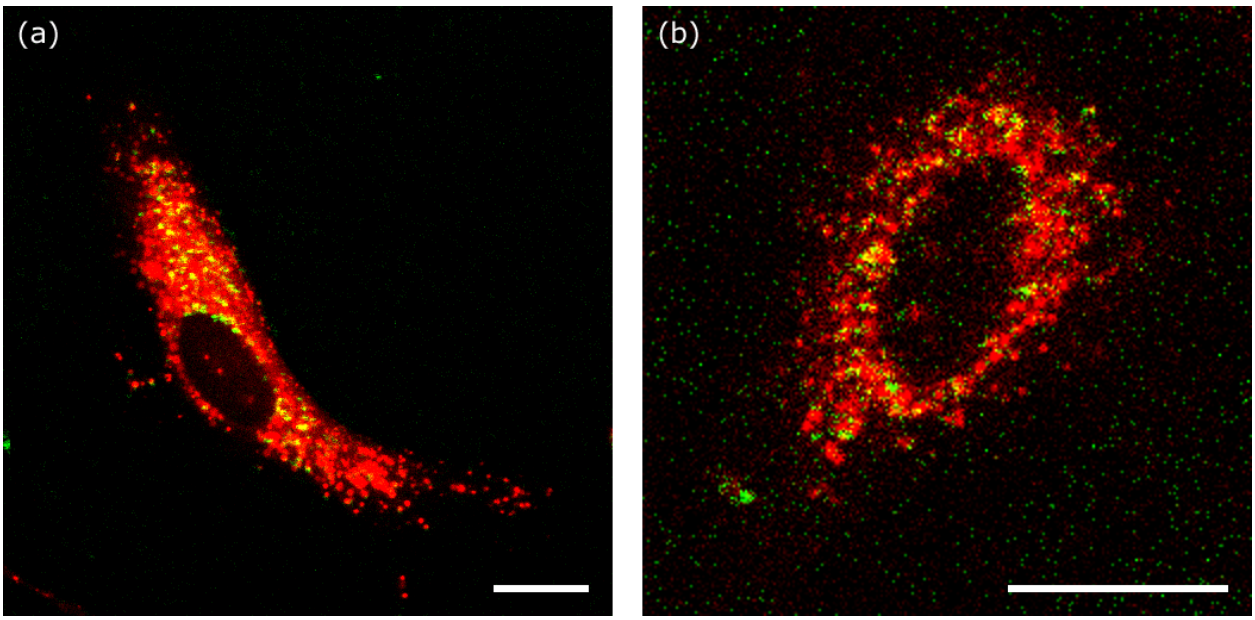

Figure S11: Colocalization measurement between the $LiNbO_3$ NPs and (a) the lysosomes and (b) the endosomes. The SHG signal from the NPs (green) was generated with the Mai Tai at 810 nm. The fluorescence from the lysosome and endosome staining (red) was excited with an Ar–ion laser at 488 nm. 20x/NA 0.8 objective. The yellow color indicates overlap. Temperature 37 $^{\circ}C$. Scale bars 20 μm. (a) Pixel dwell time 32.8 μs, pixel size 249 nm. (b) Pixel dwell time 65.5 μs, pixel size 216 nm.

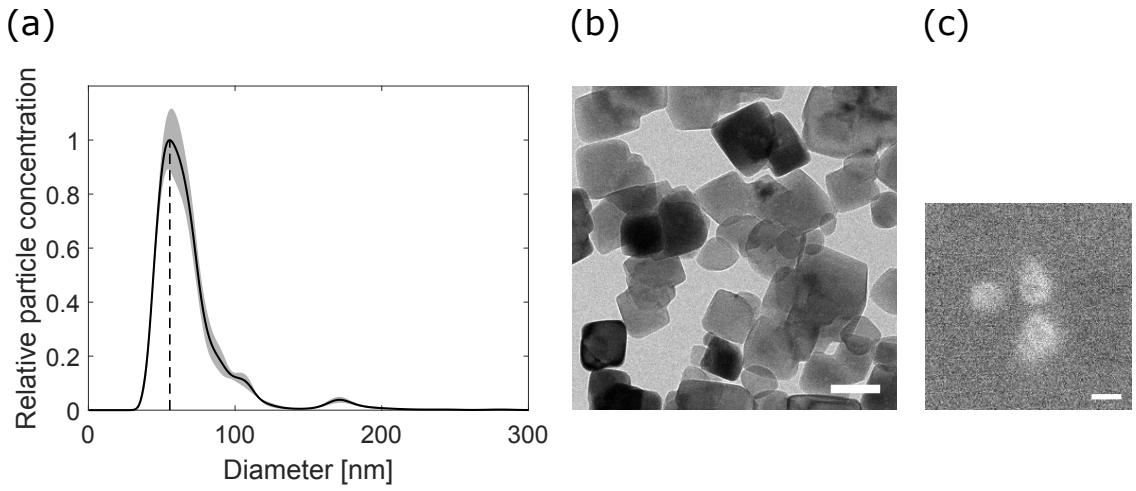

Figure S12: (a) Distribution of the diameter of the $LiNbO_3$ HNPs in water, measured with a NanoSight NS300 NP tracking analysis device. The movement of the NPs is translated into a particle size based on the Stokes–Einstein equation and the viscosity of the medium. Averaged over 5 x 60 seconds of measurement time, sCMOS camera at 25 frames per second, green laser (532 nm), slider gain 366, 5 x 1498 frames. The gray area indicates the standard error of the mean. (b) Transmission electron microscopy image of the HNPs. Scale bar 50 *nm*. (c) Scanning electron microscopy image of the same spot as in Fig. 2 (a), showing three HNPs. Scale bar 50 *nm*.

Autocorrelation sorting protocol

Input

(m x m x n) autocorrelation matrix G with m the number of data points in the ξ and ψ direction and n the number of frames in the time series.

Protocol

1. Create an empty list G_sort for storing the indices of the frame numbers from good to bad. The quality of a frame is considered to be higher when the corresponding ACF matches more closely the average ACF of all other frames.

2. if $n \geq 100$:

   (a) Calculate the average ACF $\langle G \rangle$. $\langle G \rangle$ is an (m x m) matrix.

   (b) Calculate for each ACF the value dG, the overall mean squared difference from $\langle G \rangle$. dG is a scalar.

   (c) Find the 1 % highest dG values and the corresponding frame numbers

   (d) Add the frame numbers to G_sort

   (e) Remove these frames from G, n is now equal to the remaining number of frames

   (f) Repeat step 2 until n < 100

3. if $n < 100$:

   (a) Calculate for each frame i (from 1 to n) the average ACF of all other frames. Store these together in an (m x m x n) matrix $\langle G \rangle$.

   (b) Calculate for each ACF i (from 1 to n) dG, the overall mean squared difference from $\langle G \rangle (:, :, i)$. dG is a scalar.

   (c) Find the highest dG value and the corresponding frame number

(d) Add the frame number to G_sort

(e) Remove the frame from G, n is now equal to the remaining number of frames

(f) Repeat step 3 until $n == 1$

4. Flip G_sort to change the list from good to bad

Output

(m x m x n) autocorrelation matrix G_sort, sorted from good to bad.[S1]

The distinction between $n \geq 100$ and $n < 100$ is made to speed up the computation. For large n values, the overall average autocorrelation is almost identical to the result obtained when the i–th frame is left out. Instead of throwing out only the worst autocorrelation, one can in addition remove the 1 % worst autocorrelations in a single step.

The Matlab script with the sorting algorithm may be made available upon contacting the authors.

Table S1: LSM 880 instrumental settings for the $LiNbO_3$ cRICS measurements. Pixel size 166 *nm*, 256 x 256 pixels per image. The beam waist is extracted from the fastest three measurements (6–8) to make sure that the pixel dwell time is much shorter than the characteristic rotational diffusion time. The diffusion coefficient is measured from experiments 5–8. The $\psi \neq 0$ lines in scans 1–4 are not suitable for analysis due to the low G values, *i.e.* close to the noise level, caused by the long line scan times.

Measurement number	Scan speed $[\mu m/s]$	Pixel dwell time $[\mu s]$	Number of frames	Total acquisition time [minutes]
1	936	177	50	23
2	1267	131	100	33
3	2534	65.5	150	25
4	5068	32.8	200	17
5	10135	16.4	400	17
6	20270	8.19	800	17
7	40540	4.10	1600	17
8	54054	3.07	2000	16

References

(S1) Ries, J.; Bayer, M.; Csucs, G.; Dirkx, R.; Solimena, M.; Ewers, H.; Schwille, P. Automated suppression of sample-related artifacts in Fluorescence Correlation Spectroscopy. *Opt. Express* **2010**, *18*, 11073–11082.